Propagating the measured rates backward in time, one can estimate the total amount of carbon dioxide and water, $\Delta M(CO_2)$ and $\Delta M(H_2O)$, lost through this particular channel over 3.5 gigayears (Gy) (supporting online text).

$\Delta M(CO_2)$ = 0.2 – 4 mbar over 3.5 Gy
$\Delta M(H_2O)$ < few cm over 3.5 Gy

Using a hybrid code, Modolo *et al.* (*16*) calculated the escape rates for O^+ and O_2^+ for different solar conditions. The calculated total escape rate for the heavy ions (O^+ and O_2^+) is $5.7{\cdot}10^{23}$ s^{-1}, compared to $3.1{\cdot}10^{23}$ s^{-1} in this study; i.e., the calculated and measured rates are in very good agreement. Also, the measured escape rates are in very good agreement with MHD (magnetohydrodynamics) simulations by (*17*). They provide the rates $Q(O^+) = 2.5{\cdot}10^{23}$ s^{-1}, $Q(O_2^+) = 2.9{\cdot}10^{23}$ s^{-1}, $Q(CO_2^+) = 3.1{\cdot}10^{22}$ s^{-1} for the solar minimum conditions. As can be seen, even mass composition is quite well reproduced.

Because the calculated escape rates are in good agreement with the measured ones at the solar minimum conditions, we can thus rely on the calculated factor of the escape increase for the solar maximum conditions. Modolo *et al.* (*16*) predicted the factor to be 4.56 for the O^+ escape-rate increase, and Ma *et al.* (*17*) predicted the same factor to be 4.58. Scaling the measured rates on this factor brings the total escaped amount of carbon dioxide to 0.8 to 43 mbar, and the upper limits for water to 4 to 70 cm. Thus, we conclude that the solar-activity variations cannot increase the estimated total escape on a factor of 100 needed for evolutionary relevant numbers.

The estimated total losses of carbon dioxide and water are much lower than the few hundred meters of H_2O and 1 to 5 bar of CO_2 required for the "wet and warm early Mars" model. Therefore, either other escape channels were or are operational, e.g., impact atmospheric removal, photochemical or cold plasma/bulk escape, or water and carbon dioxide are stored in nonidentified reservoirs.

We emphasize that this study considers only one channel for the escape to space. The determination of the escape rates in the form of cold plasma clouds (bulk escape) or via sputtering and photochemical reactions is beyond the scope of the ASPERA-3 experiment capabilities. To compare the measured escape rates with the other escape channels, we determined logarithm-averaged oxygen escape rates over all available models given in the review (*18*). The photochemical O^+ escape rates are estimated to be $2{\cdot}10^{25}$ s^{-1} on average; the sputtering, $7{\cdot}10^{23}$ s^{-1}; and the bulk/cold plasma escape, $1{\cdot}10^{26}$ s^{-1} [Phobos-2 database (*18*)]. As can be seen, at least in simulations, estimated photochemical or cold plasma escape rates are substantially higher than the reported numbers. Precise measurements of the cold plasma, photochemical, and sputtering escape rates must await future missions.

References and Notes

1. C. P. McKay, C. R. Stoker, *Rev. Geophys.* **27**, 189 (1989).
2. J. F. Kasting, *Icarus* **94**, 1 (1991).
3. J.-P. Bibring *et al.*, *Science* **307**, 1576 (2005).
4. S. W. Squyres *et al.*, *Science* **306**, 1709 (2004).
5. R. Lundin *et al.*, *Science* **305**, 1933 (2004).
6. M. H Acuña *et al.*, *Science* **279**, 1676 (1998).
7. E. Dubinin *et al.*, *Icarus* **182**, 343 (2006).
8. E. Dubinin, R. Lundin, O. Norberg, N. Pissarenko, *J. Geophys. Res.* **98**, 3991 (1993).
9. E. Carlsson *et al.*, *Icarus* **182**, 320 (2006).
10. R. Lundin *et al.*, *Geophys. Res. Lett.* **17**, 873 (1990).
11. M. Verigin *et al.*, *Planet. Space Sci.* **39**, 131 (1991).
12. S. Barabash *et al.*, in *Mars Express: The Scientific Payload*, A. Wilson, Ed. (ESA Special Publication SP-1240, 2004), pp. 121–139.
13. A short summary of the IMA sensor is available as supporting material on *Science* Online.
14. J. L. Fox, *Geophys. Res. Lett.* **24**, 2901 (1997).
15. A. Fedorov *et al.*, *Icarus* **182**, 329 (2006).
16. R. Modolo, G. M. Chanteur, E. Dubinin, A. P. Matthews, *Ann. Geophysicae* **23**, 433 (2005).
17. Y. Ma, A. F. Nagy, I. V. Sokolov, K. C. Hansen, *J. Geophys. Res.* **109**, A07211 (2004).
18. H. Lammer *et al.*, *Icarus* **165**, 9 (2003).
19. E. Kallio, *J. Geophys. Res.* **101**, 11133 (1996).

20. The ASPERA-3 experiment on the ESA Mars Express is a joint effort of 15 laboratories from 10 countries, all supported by their national agencies. We thank all involved agencies and the department and institutes hosting the efforts. We particularly thank the Swedish National Space Board for supporting the main Principle Investigator institute, and CNES for supporting the IMA calibrations at Centre d'Etude Spatiale des Rayonnements, Toulouse, France. We are indebted to members of the European Space Agency (ESA) for their courage to embark on a mission like Mars Express and for rapidly developing a space probe to Mars, the first ESA mission to the red planet. The interplanetary electric field proxies were based on the Mars Global Surveyor MAG/ER (Magnetometer/Electron Reflectometer) measurements (Principal Investigator M. Acuno, NASA Goddard Space Flight Center, Greenbelt, MD, USA).

Supporting Online Material

www.sciencemag.org/cgi/content/full/315/5811/501/DC1
Materials and Methods
Figs. S1 and S2
References and Notes

25 August 2006; accepted 4 December 2006
10.1126/science.1134358

Slow Earthquakes Coincident with Episodic Tremors and Slow Slip Events

Yoshihiro Ito,* Kazushige Obara, Katsuhiko Shiomi, Shutaro Sekine, Hitoshi Hirose

We report on the very-low-frequency earthquakes occurring in the transition zone of the subducting plate interface along the Nankai subduction zone in southwest Japan. Seismic waves generated by very-low-frequency earthquakes with seismic moment magnitudes of 3.1 to 3.5 predominantly show a long period of about 20 seconds. The seismicity of very-low-frequency earthquakes accompanies and migrates with the activity of deep low-frequency tremors and slow slip events. The coincidence of these three phenomena improves the detection and characterization of slow earthquakes, which are thought to increase the stress on updip megathrust earthquake rupture zones.

Nonvolcanic deep low-frequency (*1*) tremors and slow slip events (*2–4*) occur simultaneously in the transition zone (*5*) from locked to aseismic slips at the downdip portion of the Nankai subduction zone in southwest Japan. Megathrust earthquakes with seismic moment magnitudes exceeding 8 occur in this region periodically on ~100-year time scales (*6*). There is also a large gap in the source time properties of two recently discovered mechanisms of relaxation of accumulated stress in the transition zone: Deep low-frequency tremors (*1*) predominantly show frequencies near 0.5 s, suggesting that the characteristic time scale of the rupture duration is on the order of 1 s, whereas slow slip events (*2–4*) do not radiate any seismic waves and cause crustal deformations that continue for 2 to 5 days.

Deep low-frequency tremors and slow slip events in Japan have been detected by the seismic network of the National Research Institute for Earth Science and Disaster Prevention (NIED), which comprises a network of ~750 high-sensitivity seismograph network (Hi-net) and 73 broadband seismograph network (F-net) stations (*7*). The Hi-net stations provide a high-level detectability for deep low-frequency tremors with small-amplitude signals (*1*). The Hi-net and F-net stations also detect very-low-frequency (VLF) earthquakes within the accretionary prism at the updip portion of the Nankai subduction zone (*8–10*).

A two-component high-sensitivity horizontal accelerometer with a wide frequency response range from 5 Hz to direct-current component (Hi-net TILT) is installed at each Hi-net station (*11*). The accelerometers function as tiltmeters;

National Research Institute for Earth Science and Disaster Prevention, 3-1 Tennodai, Tsukuba 305-0006, Japan.

*To whom correspondence should be addressed. E-mail: yito@bosai.go.jp

they are useful in analyzing short-term slow slip events (*2*–*4*). Hi-net TILT and F-net are also useful in calculating the moment tensor solution of local earthquakes (*12*).

To understand the stress-relaxation process in the transition zone, it is important to identify all seismic and geodetic phenomena. At present, a large gap exists between the characteristic time scales for the previously identified deep low-frequency tremors and those for slow slip events. We examined the Hi-net and F-net data with the use of various bandpass filters within an overall range of 1 to 0.005 Hz in an effort to detect unidentified long-period seismic signals radiated from the transition zone. With a bandpass filter of 0.02 to 0.05 Hz, we succeed in detecting distinct, anomalous VLF signals radiated from the transition zone near the source region of deep low-frequency tremors. These signals, observed at several Hi-net TILT and F-net stations, are best identified on the radial and vertical components. The VLF signals (Fig. 1) are accompanied by wave trains of deep low-frequency tremors. The apparent velocity estimated from their arrival times at stations with an epicentral distance exceeding 50 km is ~6 km/s, which overlaps with *P*-wave velocities in this region. This value suggests that the observed VLF signals constitute body waves.

To detect VLF seismic signals and estimate their hypocenters systematically, we adopted the grid moment tensor inversion (GMTI) approach (*13*–*15*), in which we assume that the target earthquake always occurs at a grid point that is arranged with respect to both space and time. Using this approach and continuous seismograms obtained from F-net, we calculated the point source moment tensor solution at 0.1° horizontal, 3 km depth, and 1 s interval grid-point spacing (fig. S1). First, we removed time periods that are potentially contaminated with seismic waves from teleseismic and ordinary regional earthquakes from all the GMTI solutions. Next, using the F-net and Hi-net TILT data, we applied the centroid moment tensor inversion (CMTI) approach (*12*, *15*)—in which hypocenters and fault mechanisms of the target earthquakes are calculated simultaneously—to the remaining GMTI solutions.

We detected many VLF seismic events coincident with the deep low-frequency tremors and slow slip events that occurred from January to May 2006 (table S1). These VLF events with seismic moment magnitudes of 3.1 to 3.5 are located on the belt-like distribution of deep low-frequency tremors along the strike of the subducting Philippine Sea plate (Fig. 2). Local ordinary earthquakes with the same seismic moment magnitude as these VLF events are not listed in any seismic catalog.

We compared a waveform of the VLF event with that of an ordinary earthquake at the F-net station UMJ (fig. S2). Both events have the same moment magnitude of 3.4 and almost identical epicentral distance and depth. Both events have low-frequency components with similar amplitudes in the range of 0.02 to 0.05 Hz. However, the signal of a VLF event does not constitute any high-frequency components in the range of 2 to 8 Hz. This result suggests another type of slow earthquake, which we call a VLF earthquake. Earthquakes with similar discrepancies between amplitudes measured at low and high frequencies are observed on transform faults and are identified as slow earthquakes (*16*).

The observed waveforms of VLF earthquakes are explained by thrust faulting (Fig. 2 and fig. S3). The epicenters of VLF earthquakes are confined to a narrow band bound by the surface projection of 30- to 35-km depth contours of the plate interface (Fig. 2). Moreover, their epicenters clearly overlap with the seismicity of deep low-frequency tremors. The depths of the plate interface are based on the result of the depth variation of the oceanic Mohorovičić discontinuity (the crust-mantle boundary) calculated by receiver function analysis (*17*). The thickness of the oceanic crust in this region is assumed to be ~5 km according to an active-source seismic experiment (*18*). The focal depths of VLF earthquakes are distributed across slightly wider ranges (fig. S4); the averaged depths and standard deviations are 40 ± 8 km and 35 ± 9 km in the Kii-Tokai and Shikoku regions, respectively. This wide depth range can be attributed to the depth variation with a broad peak of variance reduction calculated by CMTI (fig. S5), which suggests that the focal depth is not well constrained. However, these focal depths are roughly consistent with the subducting

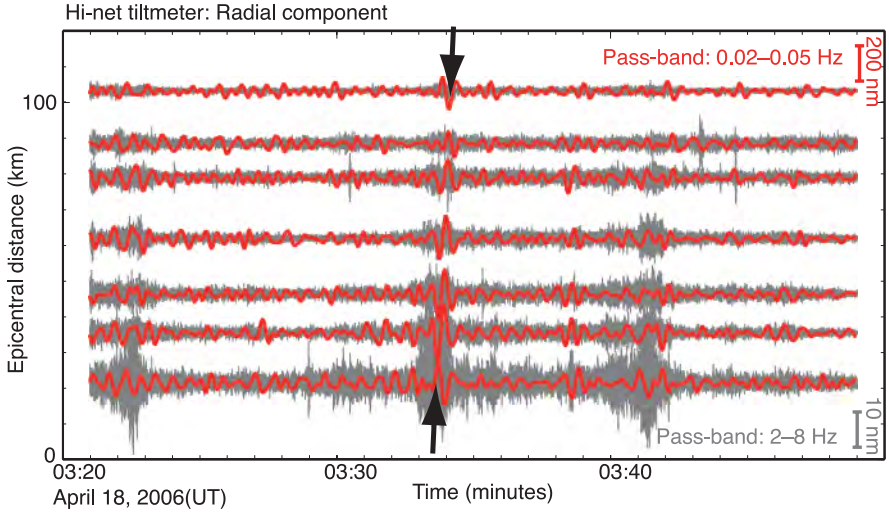

Fig. 1. Sample seismograms of a VLF earthquake at selected sites. Radial components at seven Hi-net TILT stations are shown. The observed waveforms are arranged in epicentral distance order from an estimated source location. The red and black traces represent the observed waveforms filtered for bands of 0.02 to 0.05 Hz and 2 to 8 Hz, respectively. The vertical bars on the right indicate the displacement amplitudes.

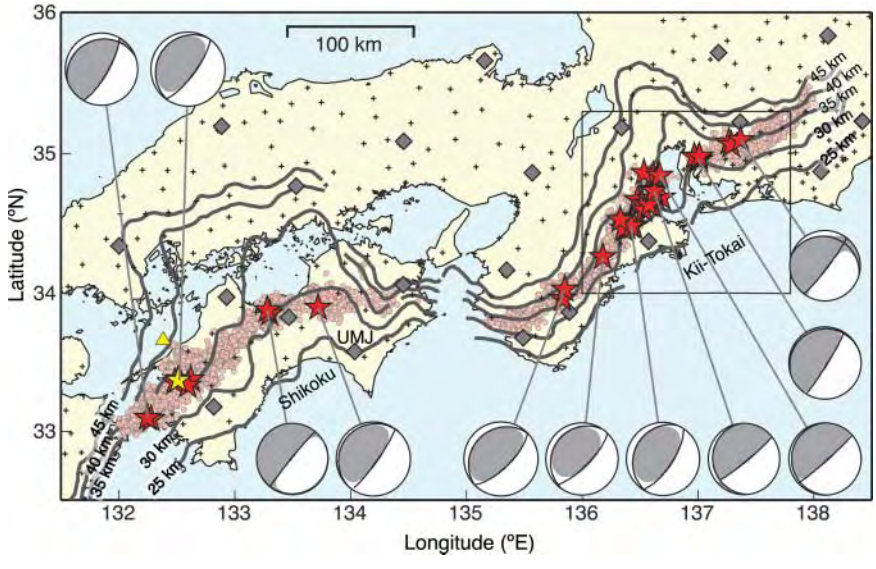

Fig. 2. VLF earthquakes (stars), deep low-frequency tremors (circles), station distribution, and moment tensor solutions of VLF earthquakes. The plus and diamond symbols represent the NIED Hi-net and F-net stations, respectively. The depth contour indicates the upper surface of the Philippine Sea plate. The rectangle indicates the area shown in Fig. 3. The yellow triangle indicates the epicenter of an ordinary earthquake with a moment magnitude of 3.4.

plate interface. The dip angles of the nodal planes dipping landward are consistent with the slope of the Philippine Sea plate; the averaged dip angles and standard deviations are 14° ± 8° in the Kii-Tokai region and 15° ± 9° in the Shikoku region. These values imply that VLF earthquakes may occur on the subducting plate interface.

The simultaneous occurrence of deep low-frequency tremors and slow slip events has been observed in southwest Japan (*2*). These activities are coincident both spatially and temporally, and they exhibit a clear migration pattern when the activity of deep low-frequency tremors is high (*4*). A clear northeastward migration of the seismicity of deep low-frequency tremors and geodetic deformations by a slow slip event were observed in the Kii-Tokai region in January 2006 (*19*). Concurrently, an identical migration of the seismicity of VLF earthquakes was observed in the same region (Fig. 3). The migration pattern of VLF earthquake seismicity is consistent with both the deep low-frequency tremor activity and the observation of the geodetic deformations. This observation indicates a close relationship between slow slip events and the activity of both VLF earthquakes and deep low-frequency tremors, thereby reflecting the stress accumulation and relaxation process in the transition zone.

The excitations of wave trains caused by VLF earthquakes appear to always overlap with the peak amplitude of wave trains caused by deep low-frequency tremors (Fig. 1). However, it should be noted that deep low-frequency tremors occur without the excitation of VLF earthquakes. This result suggests that the VLF event and the deep low-frequency tremors are two distinct phenomena.

Considering the predominance of VLF components of ~20 s (Fig. 1 and fig. S2), their response to the rupture process may correspond to a slow earthquake with a characteristic time scale of rupture duration on the order of 10 s. This rupture duration is longer than that of ordinary earthquakes and also exceeds the duration proposed for deep low-frequency tremors, ~1 s (*1*). However, this 10-s duration is obviously shorter than the 2- to 5-day duration of regionally observed slow slip events (*2*–*4*). Similar VLF earthquakes that occur within the accretionary prism are thought to represent slow earthquakes with low stress drops, low rupture velocities, and low slip velocities on the fault plane with high pore-fluid pressure (*10*). These observations suggest that three types of slow earthquakes—deep low-frequency tremors, VLF earthquakes, and slow slip events—occur simultaneously in the transition zone of the subducting plate interface.

Tomography studies that image seismic velocity structure show that a high Poisson's ratio exists around the source region of the deep low-frequency tremor (*20*). A recent precise study in the Nankai subduction zone proposes a linear distribution of low-frequency earthquakes, similar to the classification of deep low-frequency tremors with slightly obvious *P* and *S* phases, at 35 to 40 km around the plate interface and corresponding to a zone of high Poisson's ratio in the vicinity of the transition zone. This suggests the following two interpretations: (i) generation of low-frequency earthquakes by shear slip, and (ii) formation of a region of high pore-fluid pressure due to the fluid released from the dehydration of the subducted oceanic crust (*21*). Considering that three types of slow earthquakes including low-frequency earthquakes occur in the transition zone (Fig. 4), the existence of a zone of high pore-fluid pressure may play an important role in the occurrence of these slow earthquakes. One possible scenario of the stress-relaxation process in the transition zone is based on an asperity model (*22*, *23*), in which stronger coupled patches of VLF earthquakes are surrounded by aseismic slow slip regions. The fault shear strength of the slow slip segment is weaker than that of the asperity of a megathrust earthquake because the high pore-fluid pressure causes a reduction in the normal stress on the plate interface. If the shear stress loaded by the subducting plate reaches the yield stress of the bulk for the slow slip segment, the slow slip event starts in the transition zone. When the shear stress increases on the patches of VLF earthquakes due to the occurrence of the slow slip event, these patches eventually rupture after the cumulative stress reaches the yield stress reduced by the high pore-fluid pressure. This rupture results in a low stress drop and possibly induces the behavior of a VLF earthquake. Many new microcracks, with shear strength weaker than that of ordinary microearthquakes and source size smaller than that of VLF earthquakes, may rupture in the transition zone as a result of the local stress change around the plate interface, induced by the

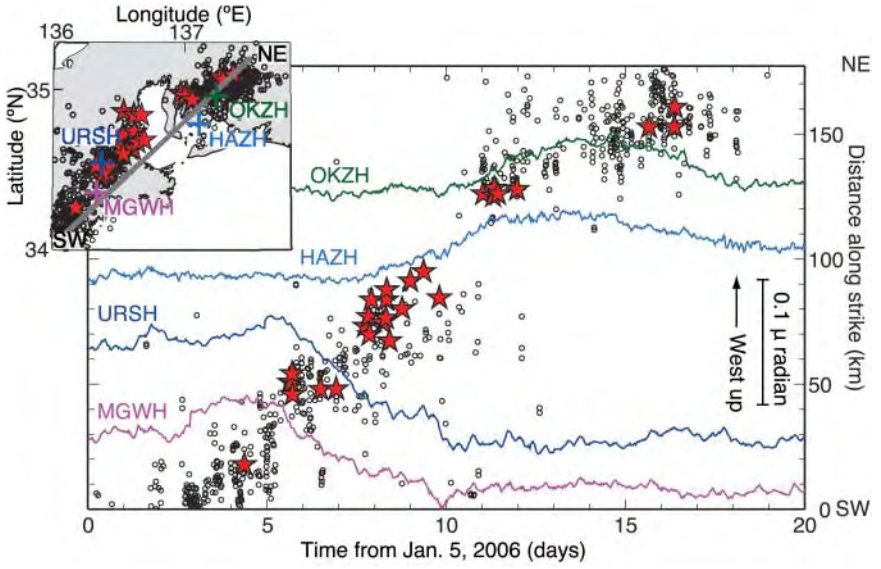

Fig. 3. Migration of seismicity of both VLF earthquakes and deep low-frequency tremors, and tilt change at four Hi-net stations—OKZH, HAZH, URSH, and MGWH—between 5 January and 25 January 2006. The temporal variation of VLF earthquakes (red stars) and deep low-frequency tremors (circles) is shown along the southwest-northeast line in the inset representing the strike of the subducting plate interface. The four colored lines are records of the east-west component of the tilt changes observed at Hi-net stations. The inset shows the distribution of the VLF earthquakes and deep low-frequency tremors during the same period, as well as the Hi-net TILT station locations (plus symbols).

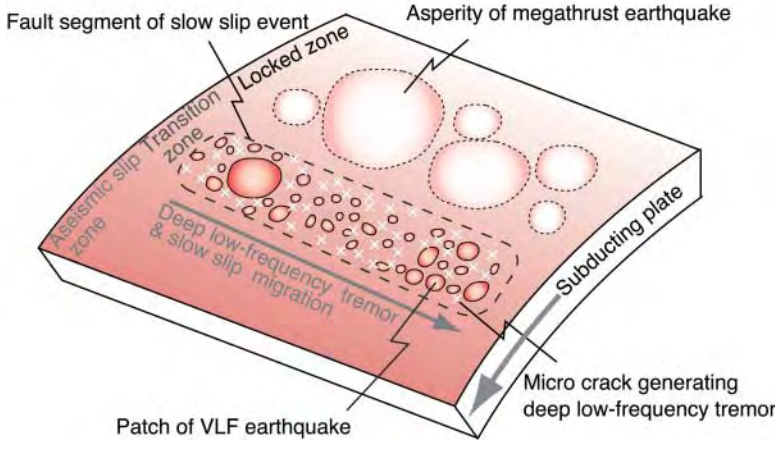

Fig. 4. Schematic of the seismic source distribution for VLF earthquakes, deep low-frequency tremors, and slow slip events at the downdip portion of the subduction zone in southwest Japan.

migration slow slip. The superposition of a seismic signal from each small failure yields the observed sequence of deep low-frequency tremors. Low-frequency tremors in the Cascadia subduction zone have an extensive depth distribution from 10 to 40 km, where there are strong seismic refractors, suggesting the existence of fluid (*24*). These tremors also may be caused by the stress change outside the transition zone due to a slow slip event, because a similar migration of the tremor seismicity and slow slip is observed in the Cascadia subduction zone (*25*).

The monitoring of not only deep low-frequency tremors but also VLF earthquakes may be useful to assess the stress on the rupture zone of a megathrust earthquake. This is because the shear stress on the asperity of the megathrust earthquake may increase as a result of slow earthquakes of all sizes occurring at the downdip portion of the subduction zone. VLF earthquakes are also useful indicators for estimating the stress condition of the rupture zone of an anticipated megathrust earthquake.

References and Notes

1. K. Obara, *Science* **296**, 1679 (2002).
2. K. Obara, H. Hirose, F. Yamamizu, K. Kasahara, *Geophys. Res. Lett.* **31**, 10.1029/2004GL020848 (2004).
3. H. Hirose, K. Obara, *Earth Planets Space* **57**, 961 (2005).
4. K. Obara, H. Hirose, *Tectonophysics* **417**, 33 (2006).
5. R. D. Hyndman, K. Wang, M. Yamano, *J. Geophys. Res.* **100**, 15373 (1995).
6. M. Ando, *Tectonophysics* **25**, 69 (1975).
7. Y. Okada *et al.*, *Earth Planets Space* **56**, xv (2004).
8. K. Obara, Y. Ito, *Earth Planets Space* **57**, 321 (2005).
9. Y. Ito, K. Obara, *Geophys. Res. Lett.* **33**, 10.1029/2005GL025270 (2006).
10. Y. Ito, K. Obara, *Geophys. Res. Lett.* **33**, 10.1029/2006GL025883 (2006).
11. K. Obara *et al.*, *Rev. Sci. Instrum.* **76**, 10.1063/1.1854197 (2005).
12. Y. Ito *et al.*, *Geophys. J. Int.* **167**, 1317 (2006).
13. H. Kawakatsu, *Bull. Earthq. Res. Inst.* **73**, 267 (1998).
14. F. Tajima, C. Megnin, D. S. Dreger, B. Romanowicz, *Bull. Seismol. Soc. Am.* **92**, 739 (2002).
15. See supporting material on *Science* Online.
16. E. A. Okal, L. M. Stewart, *Earth Planet. Sci. Lett.* **57**, 75 (1982).
17. K. Shiomi, H. Sato, K. Obara, M. Ohtake, *J. Geophys. Res.* **109**, 10.1029/2003JB002774 (2004).
18. S. Kodaira *et al.*, *Science* **304**, 1295 (2004).
19. S. Sekine, K. Obara, H. Hirose, paper presented at the Japan Geoscience Union Meeting 2006, Chiba, Japan, 14 May 2006.
20. K. Shiomi, K. Obara, H. Sato, *Tectonophysics* **420**, 205 (2006).
21. D. R. Shelly, G. C. Beroza, S. Ide, S. Nakamula, *Nature* **442**, 188 (2006).
22. T. Lay, H. Kanamori, in *Earthquake Prediction*, D. Simpson, P. Richards, Eds. (American Geophysical Union, Washington, DC, 1981), pp. 579–592.
23. R. L. Wesson, W. L. Ellsworth, *J. Geophys. Res.* **78**, 8527 (1973).
24. H. Kao *et al.*, *Nature* **436**, 841 (2005).
25. G. Rogers, H. Dragert, *Science* **300**, 1942 (2003); published online 8 May 2003 (10.1126/science.1084783).

26. We thank T. Maeda, A. Hutko, and J. Rokosky for their extensive comments and discussion.

Supporting Online Material

www.sciencemag.org/cgi/content/full/1134454/DC1
Materials and Methods
Figs. S1 to S5
Table S1
References

28 August 2006; accepted 3 November 2006
Published online 30 November 2006;
10.1126/science.1134454
Include this information when citing this paper.

Strong Relationship Between DMS and the Solar Radiation Dose over the Global Surface Ocean

Sergio M. Vallina and Rafel Simó

Marine biogenic dimethylsulfide (DMS) is the main natural source of tropospheric sulfur, which may play a key role in cloud formation and albedo over the remote ocean. Through a global data analysis, we found that DMS concentrations are highly positively correlated with the solar radiation dose in the upper mixed layer of the open ocean, irrespective of latitude, plankton biomass, or temperature. This is a necessary condition for the feasibility of a negative feedback in which light-attenuating DMS emissions are in turn driven by the light dose received by the pelagic ecosystem.

Oceanic biota influence climate in the long term by shaping the biogeochemical cycles of elements essential for Earth-system functioning (such as C, O, N, P, Si, and S) (*1*–*3*) and in the short term by exchanging climate-active gases with the atmosphere (greenhouse gases, oxidant and light scavengers, and free-radical and aerosol precursors) (*4*–*8*). One of these gases is dimethylsulfide (DMS), which represents the largest natural source of atmospheric sulfur and a major precursor of hygroscopic (i.e., cloud-forming) particles in clean air over the remote oceans (*4*, *9*), thereby acting to reduce the amount of solar radiation that crosses the atmosphere and is absorbed by the ocean. A 20-year-old hypothesis (*10*) postulated that marine plankton, cloud albedo, and solar radiation can be connected through DMS production, ventilation, and oxidation in a feedback interaction; whether this feedback would be positive or negative was uncertain.

Institut de Ciències del Mar (CSIC), Passeig Marítim de la Barceloneta 37-49, 08003 Barcelona, Catalonia, Spain. E-mail: sergio.vallina@icm.csic.es (S.M.V.); rsimo@icm.csic.es (R.S.)

We wanted to explore whether DMS concentrations are linked to epipelagic ecosystem exposure to solar radiation. A monthly sampling of surface DMS concentrations, as well as biological and physical variables, was conducted during 2003 and part of 2004 at the Blanes Bay Microbial Observatory, located at 41°30′N, 2°48′E in the coastal northwest Mediterranean. We noted that the light exposure of an idealized seawater particle (and its associated dissolved substances and buoyant organisms) depends not only on the surface irradiance and its underwater attenuation but also on the depth of the mixed layer within which the particle is confined. Thus, we estimated the daily-averaged solar radiation received in the upper mixed layer (UML), or UML solar radiation dose (SRD), from measured data of the daily-averaged surface irradiance, the underwater light extinction coefficient, and the mixed layer depth (MLD) (*11*). A linear regression analysis revealed that, during the period examined, the SRD accounted for 94% of the variance of monthly surface DMS concentrations (Fig. 1).

Application of this analysis to a triannual (1992 to 1994) time series of DMS concentrations at Hydrostation S in the Sargasso Sea (*12*) (32°10′N, 64°30′W) produced similar results. Daily surface irradiances measured in Bermuda as well as MLD and extinction coefficients

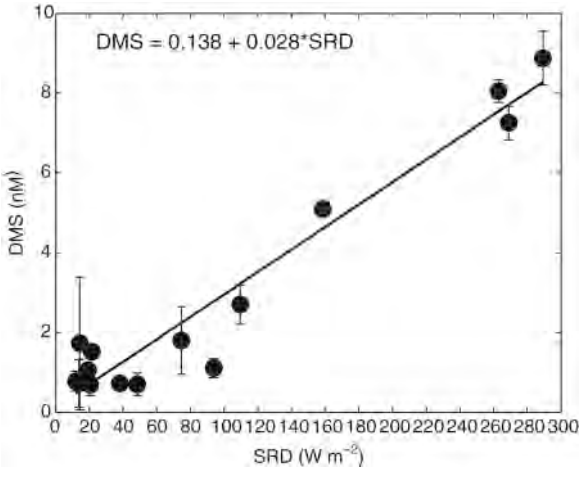

Fig. 1. Linear regression (n = 15, r^2 = 0.94) of surface DMS concentrations versus SRD in Blanes Bay (coastal northwest Mediterranean). Dots are monthly data during the period from January 2003 to April 2004. Error bars represent standard deviations of two consecutive sampling days each month. A Spearman correlation analysis of the same data gives a significant positive coefficient ρ = 0.75 (P << 0.01).